Critical phenomena at the threshold of black hole formation for collisionless matter in spherical symmetry

Ignacio (Iñaki) Olabarrieta*
Department of Physics and Astronomy, University of British Columbia, Vancouver, British Columbia, Canada V6T 1Z1

Matthew W. Choptuik†
CIAR Cosmology and Gravity Program, Department of Physics and Astronomy, University of British Columbia, Vancouver, British Columbia, Canada V6T 1Z1
and Center for Relativity, University of Texas at Austin, Austin, Texas 78712-1081
(Received 24 July 2001; published 7 December 2001)

We perform a numerical study of the critical regime at the threshold of black hole formation in the spherically symmetric, general relativistic collapse of collisionless matter. The coupled Einstein-Vlasov equations are solved using a particle-mesh method in which the evolution of the phase-space distribution function is approximated by a set of particles (or, more precisely, infinitesimally thin shells) moving along geodesics of the spacetime. Individual particles may have nonzero angular momenta, but spherical symmetry dictates that the *total* angular momentum of the matter distribution vanish. In accord with previous work by Rein, Rendall, and Schaeffer, our results indicate that the critical behavior in this model is type I; that is, the smallest black hole in each parametrized family has a *finite* mass. We present evidence that the critical solutions are characterized by unstable, *static* spacetimes, with nontrivial distributions of radial momenta for the particles. As expected for type I solutions, we also find power-law scaling relations for the lifetimes of near-critical configurations as a function of the parameter-space distance from criticality.

DOI: 10.1103/PhysRevD.65.024007 PACS number(s): 04.25.Dm

I. INTRODUCTION

Critical phenomena at the threshold of black hole formation were originally discovered in studies of the spherically symmetric, general relativistic collapse of a minimally coupled scalar field [1]. Similar behavior has now been found in many different scenarios, including the collapse of gravitational waves, perfect fluids, Yang-Mills fields and scalar fields in anti–de Sitter spacetime (for a review see [2]). Relatively little work has been done on the critical collapse of collisionless matter. To date, the only detailed study of the black-hole threshold in the Einstein-Vlasov model is due to Rein, Rendall and Schaeffer [3]. These authors found evidence that, for spherically symmetric collapse with non-zero angular momenta distributions, the threshold black hole mass is *finite* (type I behavior). In this paper we summarize the results of [4] which corroborate and extend the previous work of Rein *et al.*

The paper is organized as follows. In Sec. II, we outline the specific form of the Einstein-Vlasov equations we have solved, and make some contact with the particle-mesh (PM) method which is subsequently used to numerically solve these equations. Here we follow the approach of Shapiro and Teukolsky [5], which has been successfully used to model the dynamics of spherically symmetric, relativistic clusters of stars [6–8]. Section III describes our numerical techniques *per se*, while Sec. IV contains our main results, including evidence that the critical solutions in this model are characterized by *static* geometries and satisfy the type of scaling expected of type I solutions. Finally, some brief concluding remarks are made in Sec. V.

We use geometric units, $G=c=1$, throughout the paper. Abstract spacetime indices are generally denoted by a and b, while μ,ν and k,l are used for spacetime and spatial component indices, respectively. Finally, subscript i's label specific particles, while subscript j's are generally used for finite-difference indexing.

II. FORMALISM AND EQUATIONS OF MOTION

The dynamical state of collisionless matter can be described by a distribution function, $f(x^a,p_a)$:

$$f(x^a,p_a)=dN/dV_p \tag{1}$$

where N is the particle number and V_p is the phase-space volume. In the current case, the volume in phase space is conserved during the evolution of the system (Liouville's theorem). This implies that the distribution function is also a conserved quantity:

$$\frac{df(t,x^k,p_k)}{dt}=0. \tag{2}$$

This is the collisionless Boltzmann, or Vlasov, equation. This equation, coupled to Einstein's equations, $G_{ab}=8\pi T_{ab}$, all restricted to spherical symmetry: i.e.,

$$f(t,x^k,p_k)=f(t,R\,x^k,R\,p_k) \quad \text{with} \quad R\in SO(3) \quad k=1,2,3 \tag{3}$$

form the system we wish to solve numerically.

*Email address: inaki@physics.ubc.ca
†Email address: choptuik@physics.ubc.ca

A. Maximal-areal coordinate system

As with any problem in "3+1" ("space+time") numerical relativity, we want to specify initial data on a spatial hypersurface and then evolve these data in time. To do this, we need to split the Einstein equations into a set of constraint equations (equations that must be satisfied at each instant of time) and dynamical or evolution equations (equations that tell us how to evolve the geometric quantities in time). We carry out this splitting using the 3+1 formalism due to Arnowitt, Deser and Misner (ADM) (for reviews of this formalism, see [9] and [10]).

We restrict our attention to spherical symmetry and adopt coordinates (t,r,θ,φ) with the usual spherical-polar topology. We are left with the freedom to choose our radial and time coordinates, and have chosen maximal-areal coordinates. As the name suggests, in this system the radial coordinate is areal, so that the proper area of 2-spheres with radius r is $4\pi r^2$. The time coordinate is fixed by demanding that the $t=$const, 3-slices be *maximal*, i.e. that the trace of the extrinsic curvature, $K(t,r)\equiv K^l{}_l(t,r)$, identically vanish on each slice. This leads to a *slicing condition* on the *lapse function*, $\alpha(t,r)$, which must be satisfied at each instant of time.

With these choices, the spacetime metric takes the specific form

$$ds^2=(-\alpha(t,r)^2+a(t,r)^2\beta(t,r)^2)dt^2+2a^2\beta\,dtdr+a^2dr^2 +r^2(d\theta^2+\sin^2\theta d\varphi^2) \tag{4}$$

where $\beta(t,r)$ is the radial component of the *shift vector*, $\beta^k=(\beta,0,0)$. A sufficient set of equations for determining the geometric quantities, $a(t,r)$, $K^\theta{}_\theta(t,r)$, $\alpha(t,r)$ and $\beta(t,r)$ is then:

Hamiltonian constraint:

$$\frac{a'}{a}=\frac{3}{2}a^2rK^\theta{}_\theta{}^2+4\pi ra^2\rho+\frac{1}{2r}(1-a^2). \tag{5}$$

Momentum constraint:

$$K^\theta{}_\theta{}'=-\frac{3}{r}K^\theta{}_\theta-4\pi j_r. \tag{6}$$

Slicing condition:

$$\alpha''=\alpha'\left(\frac{a'}{a}-\frac{2}{r}\right)+\frac{2\alpha}{r^2}\left(2r\frac{a'}{a}+a^2-1\right)+4\pi a^2\alpha(S-3\rho). \tag{7}$$

Areal coordinate condition:

$$\beta=\alpha rK^\theta{}_\theta. \tag{8}$$

Here, a prime denotes differentiation with respect to r, and the last formula is derived from $\partial_t K=0$, using $K=0$. In addition, $\rho(t,r)$, $j_r(t,r)$ and $S(t,r)$, which are discussed in detail in the next section, are the local energy density, the local current density and the trace of the spatial part of the stress-energy density, respectively. We note that we have chosen to implement a *fully constrained* evolution, which in this case means that we use the constraint equations, rather than evolution equations, to update a and $K^\theta{}_\theta$.

During our simulations, we also compute the *mass aspect function*, $M(t,r)$:

$$M(t,r)=\frac{r}{2}\left(1+\frac{\beta^2}{\alpha^2}-\frac{1}{a^2}\right)=\frac{r}{2}\left(1+r^2K^\theta{}_\theta{}^2-\frac{1}{a^2}\right), \tag{9}$$

which, among other useful diagnostic purposes, allows us to detect the formation of apparent horizons. Specifically, when $2M(t,r)/r=1-1/a^2+\beta^2/\alpha^2$, becomes equal to 1, a marginally trapped surface has been formed. We can see this by computing the expansion of the outgoing null geodesics (see for instance [11]), which in these coordinates can be written as

$$1-a(t,r)r\,K^\theta{}_\theta(t,r)=1-\frac{a(t,r)\beta(t,r)}{\alpha(t,r)}. \tag{10}$$

Therefore, if the outgoing expansion is zero, $1/a^2=\beta^2/\alpha^2$, and $2M(t,r)/r=1$.

B. Stress-energy tensor

In this section we explain how we calculate the stress-energy quantities $\rho(t,r)$, $j_r(t,r)$ and $S(t,r)$ that appear in Eqs. (5)–(8). Adopting a Monte Carlo approach, we approximate the distribution function (1) by a set of N "spherical particles," which actually represent infinitesimally thin spherical shells of matter. Since these particles only interact with each other gravitationally, we have

$$T^{\mu\nu}=\sum_{i=1}^{N}T_i^{\mu\nu} \tag{11}$$

where $T_i^{\mu\nu}$ is the stress energy tensor for a single particle. For a point particle we have

$$T_i^{\mu\nu}=\frac{p_i^\mu p_i^\nu}{m_i}\,\delta(\vec{r}-\vec{r}_i(t)), \tag{12}$$

where, p_i^μ are the components of the 4-momentum of the ith particle, m_i is its rest mass, $\vec{r}_i(t)$ is its radial position at time t, and δ is the usual Dirac δ-function. In maximal-areal coordinates, the single-particle contributions to the quantities ρ, S and j_r then take the form

$$[\rho]_i=\alpha^2[T^{tt}]_i \tag{13}$$

$$[S]_i=\frac{1}{a^2}[T_{rr}]_i+\frac{1}{r^2}[T_{\theta\theta}]_i +\frac{1}{r^2\sin^2\theta}[T_{\varphi\varphi}]_i \tag{14}$$

$$[j_r]_i=\alpha[T^t{}_r]_i. \tag{15}$$

We now relax the point particle approximation and assume that each particle is a spherically symmetric shell of mass, uniformly distributed over a region Δr in radius (subsequently, Δr will be identified with the mesh spacing, h, used in the finite-difference solution of the geometrical equations). Each shell of matter is to be interpreted as an average over an ensemble of shells, each centered at $r=r_i$, and with angular momentum vectors which point in all possible directions. Thus, for any shell, the net angular momentum is zero, $\vec{l}=0$, but $|\vec{l}|^2 \equiv l^2 \neq 0$. The proper volume occupied by each particle is then given by

$$V_i = \frac{p^t}{m_i}\Delta r \int \sqrt{-g}\, d\varphi\, d\theta = 4\pi\, \Delta r\, \alpha\, a \frac{r_i^2 p_i^t}{m_i}, \tag{16}$$

and we can approximate the delta function that appears in Eq. (12) by $1/V_i$. This yields

$$\rho_i = \frac{1}{4\pi \Delta r a} \frac{[\overline{p^t}]_i}{r_i^2} \tag{17}$$

$$S_i = [S^r{}_r]_i + [S^a{}_a]_i = \frac{1}{4\pi \Delta r a^3} \frac{[p_r]_i^2}{[\overline{p^t}]_i r_i^2} + \frac{1}{4\pi \Delta r a} \frac{[l]_i^2}{r_i^4 [\overline{p^t}]_i} \tag{18}$$

$$[j_r]_i = \frac{1}{4\pi \Delta r a} \frac{[p_r]_i}{r_i^2}. \tag{19}$$

Here $[\overline{p^t}]_i$ is defined by $[\overline{p^t}]_i \equiv \alpha [p^t]_i$, and $[l]_i^2 \equiv [p_\theta]_i^2 + [p_\varphi]_i^2/\sin^2\theta_i$ is the square of the magnitude of the angular momentum of the ith particle. The geometric quantities α and a are evaluated at $r=r_i$ as described in Sec. III C. Note that we have also defined

$$S^a{}_a \equiv S^\theta{}_\theta + S^\varphi{}_\varphi \tag{20}$$

i.e., for $S^a{}_a$ the index a is summed over the *angular* coordinates. We then introduce quantities which do not explicitly depend on the geometrical quantities: $[\overline{\rho}]_i \equiv a[\rho]_i$, $[\overline{S^r}{}_r]_i \equiv a^3 [S^r{}_r]_i$, $[\overline{S^a}{}_a]_i \equiv a[S^a{}_a]_i$ and $[\overline{j_r}]_i \equiv a[j_r]_i$. In our numerical implementation of the equations of motion, these definitions provide a clean separation of the particle updates and the updates of the geometry variables.

We interpolate the one-particle quantities to the continuum and sum over all the particles to find the total values:

$$\overline{f}(r) = \sum_{i=1}^{N} \overline{f}_i W(r - r_i), \tag{21}$$

where $\overline{f}_i$ is any of the single-particle barred quantities defined above, $\overline{f}$ is the corresponding continuum quantity, and $W(r-r_i)$ is an interpolation function defined in detail in Sec. III C [see Eq. (51)]. Having defined Eq. (21) we can now write Eqs. (5)–(8) as

$$\frac{a'}{a} = \frac{1-a^2}{2r} + \frac{3}{2} r a^2 K^\theta{}_\theta{}^2 + 4\pi a r \overline{\rho} \tag{22}$$

$$K^\theta{}_\theta{}' = -\frac{3}{r} K^\theta{}_\theta - 4\pi \frac{\overline{j_r}}{a} \tag{23}$$

$$\alpha'' = \alpha' \left(\frac{a'}{a} - \frac{2}{r} \right) + \frac{2\alpha}{r^2} \left(a^2 - 1 + 2r \frac{a'}{a} \right) + 4\pi a \alpha \left(\frac{\overline{S^r}{}_r}{a^2} + \overline{S^a}{}_a - 3\overline{\rho} \right) \tag{24}$$

$$\beta = \alpha r K^\theta_\theta. \tag{25}$$

C. Evolution equations

Because there are no explicit interactions between the particles, their equations of motion are just the spacetime geodesic equations (the characteristics of the Vlasov equation). These can be derived from the formula for parallel transport of a particle's four-momentum along its world line:

$$p^a \nabla_a p^b = 0. \tag{26}$$

It proves useful to recast these equations in terms of the quantities, p_r, p^t and $l^2 \equiv p_\theta^2 + p_\varphi^2/\sin^2\theta$. We can express p^r in terms of these variables as

$$p^r(t,r) = \frac{p_r(t,r)}{a^2(t,r)} - \beta(t,r) p^t(t,r). \tag{27}$$

To compute total derivatives with respect to coordinate time we use

$$\frac{d}{dt} = \frac{\partial}{\partial t} + \frac{dr}{d\tau}\frac{d\tau}{dt}\frac{\partial}{\partial r} = \frac{\partial}{\partial t} + \frac{p^r}{p^t}\frac{\partial}{\partial r}, \tag{28}$$

where here, and in the remainder of this section, τ is the particle's proper time. Applying this operator to Eq. (27) we get

$$\frac{dp^r}{dt} = \frac{1}{a^2}\frac{dp_r}{dt} - 2\frac{p^r}{a^3}\left(\frac{\partial a}{\partial t} + \frac{p^r}{p^t}\frac{\partial a}{\partial r} \right) - \beta \frac{dp^t}{dt} - p^t \left(\frac{\partial \beta}{\partial t} + \frac{p^r}{p^t}\frac{\partial \beta}{\partial r} \right). \tag{29}$$

Substituting Eqs. (27) and (29) into Eq. (26) we obtain

$$\frac{dp_r}{dt} = -\alpha \frac{\partial \alpha}{\partial r} p^t + \frac{\partial \beta}{\partial r} p_r + \frac{1}{a^3}\frac{\partial a}{\partial r}\frac{p_r^2}{p^t} + \frac{l^2}{p^t r^3}, \tag{30}$$

which is the evolution equation for p_r. To derive the evolution equation for r, we use the definition of p^r ($p^r \equiv dr/d\tau$), which after some manipulation yields

$$\frac{dr}{dt}=\frac{p_r}{a^2p^t}-\beta. \tag{31}$$

The time component of the 4-momentum, p^t, is calculated using the normalization condition $p^\mu p_\mu=-m^2$:

$$\alpha p^t=\sqrt{m^2+\frac{{p_r}^2}{a^2}+\frac{l^2}{r^2}}. \tag{32}$$

It is also convenient, as previously mentioned, to use $\overline{p^t}=\alpha p^t$ rather than p^t itself. Using this definition in Eqs. (30), (31) and (32) yields the final form of the particle equations of motion:

$$\frac{dp_r}{dt}=-\frac{\partial\alpha}{\partial r}\overline{p^t}+\frac{\partial\beta}{\partial r}p_r+\frac{\alpha}{a^3}\frac{\partial a}{\partial r}\frac{{p_r}^2}{\overline{p^t}}+\frac{l^2\alpha}{\overline{p^t}r^3} \tag{33}$$

$$\frac{dr}{dt}=\frac{\alpha p_r}{a^2\overline{p^t}}-\beta \tag{34}$$

$$\overline{p^t}=\sqrt{m^2+\frac{{p_r}^2}{a^2}+\frac{l^2}{r^2}}. \tag{35}$$

III. NUMERICAL APPROACH

As discussed in the previous section, we have adopted a Monte Carlo, particle-based strategy to the solution of the Vlasov equation. In this approach we generate an N-particle sample of some specified initial distribution function $f(0,x^k,p_k)$, and then use dynamical evolution of the N particles to approximate the full dynamics of $f(t,x^k,p_k)$. The continuum limit is recovered in the limit $N\to\infty$ and, in the absence of any sophisticated ''importance sampling'' techniques, we expect the level of statistical error in our particle calculations to be of the order of $1/\sqrt{N}$. We couple the particles to the gravitational field by introducing a finite-difference mesh on which we approximately solve the geometric equations, and by introducing transfer operators which allow us to produce mesh-based representations of particle quantities and *vice versa*. ''Particle-mesh,'' or PM, methods such as ours are commonly used in the solution of Boltzmann equations, particularly those involving long-range interactions, and the reader is referred to [12] for a detailed review of such techniques.

Here we simply note that a PM method is generically characterized by the splitting of each discrete time step, $t^n\to t^{n+1}$ into two stages: (1) the solution of the field equations on a finite-difference mesh, and (2) the updating of particle positions via discrete versions of their equations of motion. In our case, and as described in the previous section, at each time step the stress-energy quantities are calculated by considering each particle to be ''smoothed'' over a finite volume.

A. The field equations

We first explain how the equations (22)–(25) for the geometry are solved numerically, assuming that we know the quantities $\overline{\rho}$, $\overline{j_r}$, $\overline{S^r}_r$, $\overline{S^a}_a$ (our computation of the stress-energy quantities is described in Sec. III C). The first two equations, Eqs. (22), (23), are integrated from the origin, $r=0$, using the LSODA [13] integrator. The boundary conditions are given by the spherical symmetry of the spacetime, and by the demand that the spacetime be locally flat at $r=0$. They are $a(t,0)=1$, and $K^\theta{}_\theta(t,0)=0$.

We compute the values of the functions a_j and $K^\theta{}_{\theta\,j}$ on a uniform grid of N_r points, $r_j\equiv(j-1)h$, $j=1,\ldots,N_r$, where $h\equiv\Delta r=r_{\max}/(N_r-1)$, and $r=r_{\max}$ is the outer edge of the computational domain.

In order to compute the values at $r=r_{j+1}$, we supply to LSODA the values of the functions at $r=r_j$ and the derivatives computed using Eqs. (22), (23) at $r=r_{j+1/2}$, using the average of $\overline{\rho}$ and $\overline{j_r}$ at r_j and r_{j+1}:

$$[\overline{\rho}]_{j+1/2}=\frac{1}{2}([\overline{\rho}]_j+[\overline{\rho}]_{j+1}) \tag{36}$$

$$[\overline{j_r}]_{j+1/2}=\frac{1}{2}([\overline{j_r}]_j+[\overline{j_r}]_{j+1}). \tag{37}$$

Once we have calculated a, we can solve the slicing equation:

$$\alpha''=\alpha'\left(\frac{a'}{a}-\frac{2}{r}\right)+\frac{2\alpha}{r^2}\left(a^2-1+2r\frac{a'}{a}\right)+4\pi a\alpha(\overline{S^r}_r+\overline{S^a_a}-3\overline{\rho}), \tag{38}$$

with the boundary conditions

$$\alpha'(t,0)=0, \tag{39}$$

$$\alpha(t,\infty)=1. \tag{40}$$

Here the first condition follows from the demand that the slicing be regular at $r=0$, and the second one follows from asymptotic flatness, plus the demand that t measure proper time at infinity. We solve Eq. (38) using a second-order finite-difference approximation on the finite-difference mesh:

$$\frac{\alpha_{j+1}-2\alpha_j+\alpha_{j-1}}{h^2}=\frac{\alpha_{j+1}-\alpha_{j-1}}{2h}\left(\frac{a_{j+1}-a_{j-1}}{2ha_j}-\frac{2}{r_j}\right)+\frac{2\alpha_j}{{r_j}^2}\left({a_j}^2-1+2r_j\frac{a_{j+1}-a_{j-1}}{2ha_j}\right)+4\pi a_j\alpha_j\left(\frac{[\overline{S^r}_r]_j}{{a_j}^2}+[\overline{S^a_a}]_j-3[\overline{\rho}]_j\right). \tag{41}$$

Rearranging this equation gives us

$$\left(\frac{1}{h^2}+\frac{f_j}{2h}\right)\alpha_{j+1}-\left(\frac{2}{h^2}+g_j\right)\alpha_j+\left(\frac{1}{h^2}-\frac{f_j}{2h}\right)\alpha_{j-1}=0 \tag{42}$$

where

$$f_j=\frac{a_{j+1}-a_{j-1}}{2ha_j}-\frac{2}{r_j} \tag{43}$$

$$g_j=\frac{2}{r_j{}^2}\left(a_j{}^2-1+2r_j\frac{a_{j+1}-a_{j-1}}{2ha_j}\right)+4\pi a_j\left(\frac{[\overline{S^r}_r]_j}{a_j{}^2}+[\overline{S^a_a}]_j-3[\overline{\rho}]_j\right). \tag{44}$$

In addition to Eq. (42) we have the boundary equation at $r=0$:

$$\left(-3+\frac{1/h^2+f_2/(2h)}{1/h^2-f_2/(2h)}\right)\alpha_1+\left(4+\frac{-2/h^2-g_2}{1/h^2-f_2/(2h)}\right)\alpha_2=0, \tag{45}$$

which can be derived from the $O(h^2)$ forward finite-difference approximation to $\alpha'=0$ at $r=0$

$$\frac{-3\alpha_1+4\alpha_2-\alpha_3}{2h}=0, \tag{46}$$

and Eq. (42) with $j=2$. We have also the boundary condition at $r=r_{\max}$:

$$\alpha_{N_r}=\sqrt{1-\left(\frac{2M_{N_r}}{r_{N_r}}\right)} \tag{47}$$

where M is the mass aspect function defined by Eq. (9). This approximation follows from the known representation of the asymptotically-flat Schwarzschild solution in maximal-areal coordinates. Equations (42), (45) and (47) constitute a linear tridiagonal system that can be solved using a tridiagonal solver (we have used the LAPACK [14] routine DGTSV).

B. The evolution equations

To evolve the particles' positions and momenta we integrate the geodesic equations (33), (34). The values of the coefficients in these equations (basically products and quotients of a, α, β, a', α' and β') must be calculated at the particle positions, r_i, using the values obtained at the mesh points, r_j. The mesh values are interpolated to the particle positions using the same operator kernel used to produce mesh values from particle quantities (this procedure is explained in the next section). The geodesic equations are also integrated using the LSODA routine. At discrete time $t=t^n$, given a particle's position, r^n, and radial momentum, p_r^n, we calculate the new position, r^{n+1}, and momentum, p_r^{n+1}, at $t=t^{n+1}=t^n+\Delta t$ by supplying to LSODA the values of the metric functions and their spatial derivatives evaluated at $t=t^n$. Because we use the $t=t^n$ values of the geometric quantities in the particle updates, rather than, for example, values at $t=t^{n+1/2}$, we expect our solution of the particle equations to have accuracy $O(\Delta t)$. We also note that in our numerical implementation, we chose a value of Δt proportional to h, i.e. $\Delta t=\lambda h$, where usually $\lambda=1.0$.

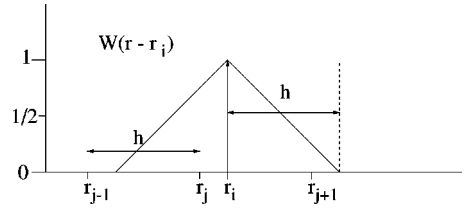

FIG. 1. Illustration of the smoothing kernel, $W(r-r_i)$. Here, r_i is the position of a particle; $\cdots r_{j-1}$, r_j, $r_{j+1}\cdots$ are the (uniform) finite-difference mesh points with $\Delta_r=r_{j+1}-r_j=\text{const}=h$.

We need to take special care if a particle leaves the computational domain ($r_i>r_{\max}$) or if it reaches the origin. In the first case we simply remove the particle from the integration scheme. When a particle reaches the origin, which operationally is signaled by $r_i<0$, we "reflect" the particle by setting

$$r_i\to -r_i, \tag{48}$$

$$[p_r]_i\to -[p_r]_i, \tag{49}$$

$$l_i\to l_i. \tag{50}$$

C. Interpolation and restriction

In this section we explain how we calculate the stress-energy quantities on the finite-difference mesh from a given set of particles (restriction), as well as how we interpolate the geometric quantities from the finite-difference mesh to the particles' positions.

The values of the stress-energy quantities $\overline{\rho}$, $\overline{j_r}$, $\overline{S}$ are calculated on the mesh using Eq. (21):

$$\overline{f}(r_j)=\sum_{i=1}^{N}\overline{f_i}W(r_j-r_i)$$

where $\overline{f_i}$ are the single particle quantities. In our implementation, we use the specific kernel (see Fig. 1):

$$W(r_j-r_i)=\begin{cases}1-|r_j-r_i|/h, & |r_j-r_i|\leqslant h,\\ 0 & \text{otherwise.}\end{cases} \tag{51}$$

Similarly, to restrict the geometric quantities calculated on the mesh to the particles' positions we compute

$$F(r_i)=\sum_{j=1}^{N_r}F(r_j)W(r_j-r_i) \tag{52}$$

where, again, r_i is the position of the particle, r_j are the grid points, and F is any of the coefficients which appear in the geodesic equations. These coefficients are generally products and quotients of metric functions and their derivatives. In order to calculate derivatives we use the standard $O(h^2)$ finite-difference approximation:

$$[F']_j=(F_{j+1}-F_{j-1})/(2h)+O(h^2) \tag{53}$$

and then use Eq. (52) to find an approximate value for $F'(r_i)$.

D. Initial data

To initialize the sets of particles which we evolve, we specify the particle distribution (number of particles per unit of areal coordinate) and the velocity distribution (specifically the number of particles per p_r and l). This corresponds to a *separable* distribution function, $f(r,p_r,l)$:

$$f(r,p_r,l)=R(r)P(p_r)L(l). \tag{54}$$

Moreover, instead of specifying P as a function of p_r we give $P=P(\bar{p_r})$ where $\bar{p_r}=p_r/a$. This allows us to calculate the value of $p^t=\sqrt{m^2+\bar{p}_r^2+l^2/r^2}$ (assuming all the particles have the same rest mass m), and therefore $[\bar{\rho}]_i$, $[\bar{j_r}]_i$ and $[\bar{S}]_i$ without *a priori* knowledge of the geometry. We can thus decouple the tasks of specifying initial conditions for the particles, and ensuring that the constraints are satisfied at $t=0$.

We use 1-dimensional Monte Carlo techniques applied to each of $R(r)$, $P(p_r)$, $L(l)$ to get a specific set of N particles. As mentioned above, the statistical error, in theory, should scale as $1/\sqrt{N}$.

IV. RESULTS

All of the calculations discussed in this paper were performed with $N_r=257$, $N=10^5$ and $h=0.078125$. With this choice of parameters we ensured that the truncation error due to the finite-differencing of the field equations with mesh spacing h was of the same order of magnitude as the statistical error resulting from representation of the phase-space distribution with a finite number, N, of particles. We have observed [4] that both types of error scale in the expected way: the truncation error scales as $O(h)$, with the number of particles per cell fixed; the statistical error scales as $1/\sqrt{N}$ for fixed h, and as $O(1/h)$ for fixed N. Once the two errors are of comparable magnitude, in order to further decrease the overall error (truncation plus statistical error) as $O(h)$, we have to increase the number of particles as $N\approx 1/h^4$. This scaling behavior makes it very costly to substantially reduce the level of numerical error in the results presented here.

Our critical solutions (solutions sitting at the threshold of black hole formation) were found by performing bisection searches using the total rest mass, M_0:

$$M_o=\sum_{i=1}^{N} m_i=Nm \tag{55}$$

as the tuning parameter. In particular, if $M_o^\star$ is the critical parameter value, then configurations with $M_o<M_o^\star$ (subcritical) will eventually disperse, while those with $M_o>M_o^\star$ (supercritical) will form black holes. For any given critical search, we generally determined $M_o^\star$ to a relative precision of about 4×10^{-11}. Table I provides a summary of the various families we have studied.

TABLE I. Summary of critical searches described in the text. Listed are family label, form of initial data, set number (for families where multiple, independent, N-particle representations of the initial distribution function were used) and computed lifetime-scaling exponents, σ. See the text and particularly Eqs. (56)–(58) and (63),(64), respectively, for detailed definitions of the "Gaussian" and "Tanh" initial data. Also note that ATS stands for "almost time symmetric," as discussed in the text. The quoted error for *all* values of σ is the estimated statistical error for the ATS data [see Eq. (62)].

Family	Form of initial data	Set no.	σ
(a)	Gaussian, $l_o=12$ ATS	1	5.1 ± 0.2
(a)	Gaussian, $l_o=12$ ATS	2	5.3 ± 0.2
(a)	Gaussian, $l_o=12$ ATS	3	5.2 ± 0.2
(b)	Gaussian, $l_o=3$	1	5.7 ± 0.2
(c)	Gaussian, $l_o=5$	1	5.5 ± 0.2
(d)	Gaussian, $l_o=7$	1	5.0 ± 0.2
(d)	Gaussian, $l_o=7$	2	5.0 ± 0.2
(e)	Gaussian, $l_o=12$	1	4.9 ± 0.2
(f)	Tanh, $l_o=7$	1	5.9 ± 0.2

We first focus on a specific family of initial conditions [Table I, family (a)] and then summarize our observations for the remaining families. We thus consider an initial distribution defined by

$$R(r)=r^2 e^{(-(r-r_o)^2/\Delta_r^2)}\Theta(r) \tag{56}$$

$$P(\bar{p_r})=e^{(-(\bar{p_r}-\bar{p}_{ro})^2/\Delta_{\bar{p}_r}^{-2})} \tag{57}$$

$$L(l)=e^{(-(l-l_o)^2/\Delta_l^2)}\Theta(l) \tag{58}$$

where, again, $\bar{p_r}=p_r/a$, and Θ is the step function. We take $r_o=5$, $\Delta_r=1$, $\bar{p}_{ro}=0$, $\Delta_{\bar{p}_r}^{-}=2$, $l_o=12$, $\Delta_l=2$, and refer to the data as "almost time symmetric" (ATS) since the Gaussian for the radial momentum is centered at $p_r=0$. The critical parameter for this family is $M_o^\star\approx 1.3$ as shown in Fig. 2. This figure also shows that the smallest black hole formed has *finite* mass and that the transition is therefore of type I, in agreement with the observations of Rein *et al.* [3].

In Fig. 3 we show a few snapshots of the evolution of $\dot{a}(t,r)\equiv\partial_t a(t,r)$ resulting from initial data which is close to criticality but which eventually disperses. At early times, $\dot{a}(t,r)$ oscillates, but for $100\lesssim t\lesssim 200$ it appears to approach 0. In the last snapshot ($t=234$) we observe that $\dot{a}(t,r)$ has become negative, corresponding to dispersal of the particles. We also observe similar behavior for the time derivatives $\dot{\alpha}$ and $\dot{\beta}$.

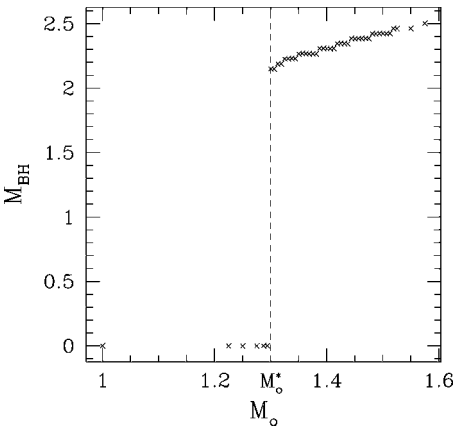

FIG. 2. Black hole mass as function of total rest mass, M_o, for the ''almost time-symmetric,'' Gaussian family of initial data described in the text [Table I, family (a)]. We observe that the smallest black hole has a finite mass (type I transition) at a critical parameter $M_o^\star \approx 1.3$ (dashed line). Computationally, we have tuned $M_o^\star$ to a relative precision of about 4×10^{-11}, which is typical of the critical surveys discussed in this paper. The discrete jumps in the black hole masses for $M_o > M_o^\star$ reflect the discrete nature of the finite-difference grid. We have made no attempt to ''interpolate'' the location of the black hole horizon in the finite-difference mesh; hence our mass estimates will always satisfy $M_{\rm BH} = k\Delta r = kh$, for some integer k.

In order to better see how small $\dot{a}(t,r)$ becomes, we show in Fig. 4 details of $\dot{a}(t,r)$ at $t=156$ for three different sets of particles sampled from the same initial distribution function. The difference between the solutions obtained with different sets give us an estimate of the statistical error, $\Delta_S(\dot{a})$, in the calculation. From the figure we can see that for the most part, $|\Delta_S(\dot{a})| \approx |\dot{a}|$. This is not the case for $r \gtrsim 5.5$ where the three calculations all seem to indicate a specific non-zero value for $\dot{a}$; however, we suspect that the amplitude of this feature may decrease if we tune closer to the critical solution, and if we use greater resolution. More importantly, the region $r \gtrsim 5.5$ accounts for only about 5–10 % of the mass of the near-critical configuration.

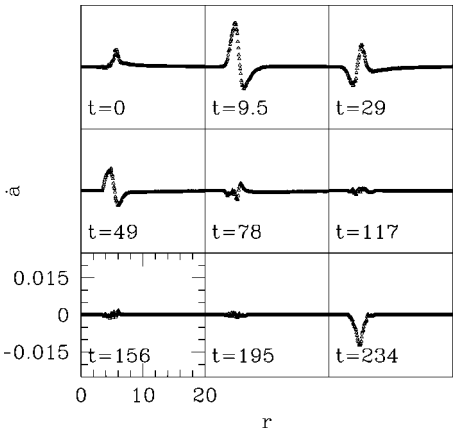

FIG. 3. Evolution of $\dot{a}$ from a marginally subcritical calculation ($M_o < M_o^\star$) using family (a). Note that at intermediate times $|\dot{a}| \approx 0$.

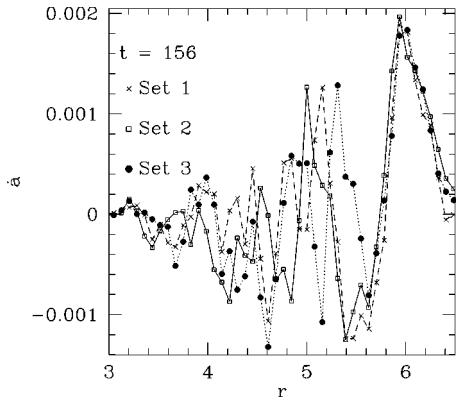

FIG. 4. Plot of $\dot{a}(156,r)$ from three separate family (a) calculations using distinct initial particle sets ($N=10^5$). The scatter in the displayed datasets gives a rough indication of the level of statistical error $\Delta_S(\dot{a})$ in the computations. The plot shows that, at least for $r \lesssim 5.5$, where 93% of the mass of the putative static cluster is located, there is little or no correlation between the three sets. Thus, any nonzero value of $\dot{a}$ in the critical limit may be attributable to finite-N statistical fluctuations.

These results are thus *consistent* with $\dot{a} \to 0$ in the critical regime, although more definitive proof would require significantly higher particle numbers, as well as higher finite-difference resolution. If we accept that the metric coefficients become independent of t in the critical regime, then the critical spacetime is stationary. If, in addition, the vector $N^a = (\partial/\partial t)^a$ is orthogonal to the spatial hypersurfaces, then the spacetime is static, and the shift function, $\beta(t,r)$, must vanish. In Fig. 5 we show the evolution of the shift function. During the period when the time derivatives of the metric coefficients are close to zero, the shift function $\beta(t,r)$ is also close to zero, in the sense that $|\Delta_S(\beta)| \approx |\beta|$. We thus have evidence that the critical solution in this case is characterized by a static geometry.

We have also observed that in the critical regime the total current density, j_r, tends to zero. This must be the case if the

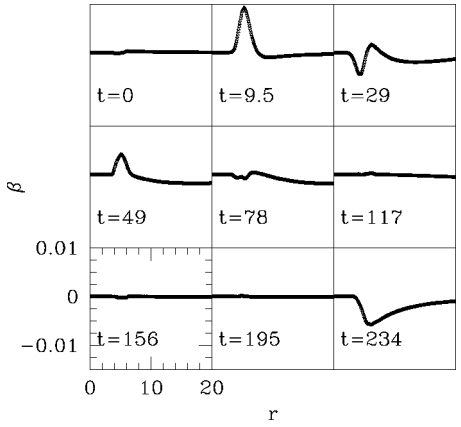

FIG. 5. Evolution of β from a marginally subcritical calculation using family (a). The shift function apparently vanishes during the same period of time as does $\dot{a}$. Therefore, during this interval, we have evidence that $N^a = (\partial/\partial t)^a$ is orthogonal to the hypersurfaces, and, thus, that the geometry is static.

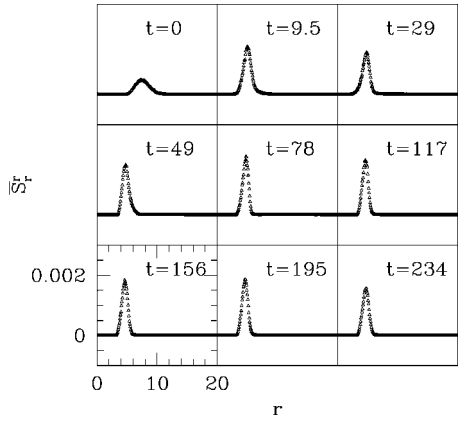

FIG. 6. Evolution of $\overline{S^r}_r(t,r)$ from a marginally subcritical calculation using family (a). During the static regime, $\overline{S^r}_r(t,r)$ is bounded away from zero, showing that although p_r is zero on average, $|p_r|$ is not.

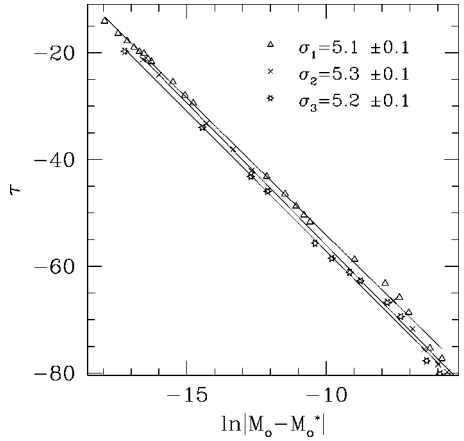

FIG. 7. Illustration of scaling law for the lifetime of near-critical configurations. The quoted uncertainty for each value of σ is the standard deviation of the slope, which has been computed using a least squares fit.

spacetime is static. However, as shown in Fig. 6, the $\overline{S^r}_r$ component of the stress energy tensor is *non-zero* near criticality. This means that although on average there are the same number of particles with positive (outward-directed) and negative (inward-directed) p_r, the mean value of $|p_r|$ does *not* vanish.

As is typical of type I critical solutions, as we tune $M_o \to M_o^\star$, the dynamical solution spends more and more time ''close'' to the putative static solution, and we expect to find power-law scaling of the time, τ (the ''lifetime'' of the near-critical configuration) spent in the critical regime as a function of $\ln|M_o - M_o^\star|$. Specifically, we expect the static critical solution (or solutions, since we are unable to demonstrate convincingly that the model has a *unique* critical solution, up to trivial rescalings) to possess exactly one unstable mode in perturbation theory, with an associated Lyapounov exponent which is simply the reciprocal of the scaling exponent, σ, in the lifetime scaling law:

$$\tau \sim -\sigma \ln|M_o - M_o^\star|. \tag{59}$$

Figure 7 shows a plot of $\tau = t - t_c$ versus $\ln|M_o - M_o^\star|$ where t is the total time that the particles in the solution generated with parameter M_o are localized within $r = r_o = 6$, and t_c is the same quantity for the solution closest to criticality. We show results from calculations using three different sets of particles and the same Gaussian family previously discussed. Using the residual scaling freedom in the model (the equations of motion are invariant under $t \to \kappa t$, $r \to \kappa r$ for arbitrary $\kappa > 0$), we have also normalized each critical solution to have unit ADM mass:

$$r \to r/M^c(t^\star, r_{\max}) \tag{60}$$

$$t \to t/M^c(t^\star, r_{\max}). \tag{61}$$

Here $t^\star$ is defined to be the instant at which the time derivatives of the metric components are closest to zero for the solution closest to criticality. $M^c(t^\star, r_{\max})$ is then the value of the mass aspect function at $t = t^\star$, $r = r_{\max}$, again for the most nearly-critical solution. We can see that there is a *rough* linear relation between the lifetime τ of the near-critical configurations and $\ln|M_o - M_o^\star|$:

$$\tau \sim -(5.2 \pm 0.2)\ln|M_o - M_o^\star| \tag{62}$$

where the quoted uncertainty is an estimate of the statistical error.

Qualitatively, then, our results are similar to what has been observed in other instances of type I critical collapse [15]. We have also found results similar to those just presented by using 4 other Gaussian families [Table I, families (b)–(e)], each with $\overline{p}_{ro} = -4$ and with varying l_o's of 3, 5, 7 and 12; $r_o = 5$, $\Delta_r = 1$, $\Delta_{\overline{p}_r} = 2$ and $\Delta_l = 2$, as for family (a). Specifically, in each case we find that the critical geometry appears to be static. We note that for smaller values of l_o, the mass in the critical solution gets increasingly concentrated near $r = 0$, making accurate evolution with a uniform finite-difference grid more difficult. Finally, we have studied a family with the following initial single-particle distributions [Table I, family (f)]:

$$R(r) \propto (1 - \tanh[(r - r_o)/\Delta_r]^2)\Theta(r) \tag{63}$$

$$P(p_r) \propto (1 - \tanh[(\overline{p}_r - \overline{p}_{ro})/\Delta_{\overline{p}_r}]) \tag{64}$$

$$L(l) \propto (1 - \tanh[(l - l_o)/\Delta_l]^2)\Theta(l). \tag{65}$$

Here we took $r_o = 5$, $\Delta_r = 1$, $\overline{p}_{ro} = -4$, $\Delta_{\overline{p}r} = 2$, $l_o = 7$ and $\Delta_l = 2$. For this data we also find evidence that as $M_o \to M_o^\star$, the geometry becomes static.

In Fig. 8 we show profiles of $2M(t^\star, r)/r$ for all of the different families considered, each separate profile being selected from the corresponding period of near-critical evolution. Again, since different initial conditions set different overall length scales for the problem, we have normalized the results using the rescaling given by Eqs. (60), (61). We see that, after normalization, the peak of $2M(t^\star, r)/r$ is *roughly* at the same radial location, $r \equiv r^\star = 2.3$. We also find

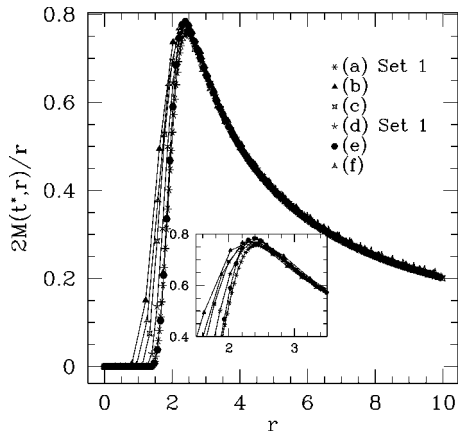

FIG. 8. Comparison of near-critical solutions for different families of initial data (Table I). We see evidence for a universal profile $2M(t^\star,r)/r$, where $t^\star$ (different for each family) is the instant when the temporal derivatives of the metric components are minimized, and r has been rescaled for each family so that all critical solutions have unit ADM mass. The maximum value of $2M(r)/r$ is about 0.76 showing immediately that the critical solution cannot be one of the clusters considered in [16], since there are no equilibrium Einstein clusters with maximum $2M(r)/r$ larger than 2/3. (Moreover, in contrast to the configurations studied here, all particles in an Einstein cluster are in circular orbits.)

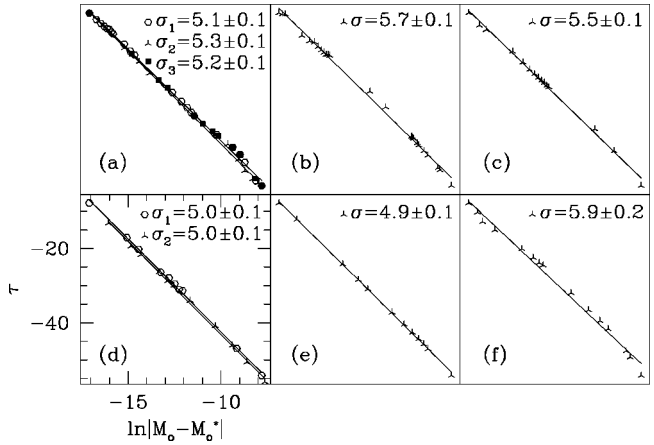

FIG. 9. Scaling behavior for different families of initial data. We observe near-critical lifetime-scaling behavior for all the families we have studied, as expected for type I solutions (static or periodic solutions, with *one* unstable mode in perturbation theory). The quoted uncertainty in σ is given by the standard deviation of the least-squares slope. The axes ranges vary somewhat from subplot to subplot; the values shown for family (d) are representative.

that the better resolved a solution is, the closer it conforms to the best resolved solution [Table I, family (a)]. This provides some indication that there may be a *universal* critical solution in this model (up to trivial rescalings, $r\to\kappa r$, $t\to\kappa t$), but again, we would need better finite-difference resolution and many more particles to verify this conjecture. This figure also shows that the maximum of $2M(t^\star,r)/r$ has a value of approximately 0.76. This immediately shows that the critical solution is not one of the clusters considered in [16], since there are no equilibrium Einstein clusters with maximum $2M(r)/r$ larger than 2/3.

We have also estimated σ defined by Eq. (59) for the different families described above. Figure 9 shows the lifetime scaling measured for the various initial data sets, where the quoted uncertainty in each value of σ is the standard deviation of the slope computed from a least squares fit. The values that we have obtained for the scaling exponents are also collected in Table I.

Finally, we are also interested in investigating the dependence of the critical solutions on the distribution of angular momentum. In Fig. 10 we show $r^2\overline{S^a}_a(t^\star,r)$ for the different families of initial data we have studied. Here

$$r^2\overline{S^a}_a = r^2\left[\sum_{i=1}^{N} W(r-r_i)\frac{1}{4\pi\Delta r}\frac{[l]_i^2}{r_i^4[\overline{p^t}]_i}\right] \qquad (66)$$

[see Eq. (18)], and $t^\star$ is defined as previously. We note that $r^2S^a{}_a(t,r)$, is a dimensionless quantity which measures the square of the angular momentum of the distribution of particles. As in Fig. 8, we have again rescaled the radial coordinate (and time) so that the critical configuration has unit ADM mass. We see that there is no obvious agreement of the profiles calculated from different families of initial data; clearly more work needs to be done in order to clarify the effect of initial angular momentum distributions on critical evolution in this model.

V. CONCLUSIONS

We have studied critical behavior at the threshold of black hole formation for collisionless matter with angular momentum and have corroborated the findings of Rein *et al.* [3] that the black holes which form at threshold in this model are of *finite* mass (type I behavior). Further, our results indicate that for families with non-zero angular momentum, the critical solution has a static geometry, with non-zero radial particle

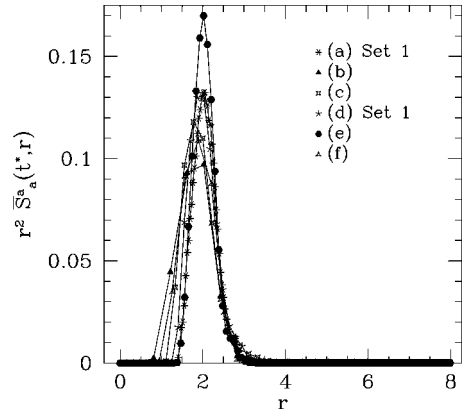

FIG. 10. $r^2\overline{S^a}_a(t^\star,r)$ for the different families in the near-critical regime. As described in the text, this quantity is a dimensionless measure of the squared-angular-momentum of the distribution. In contrast to Fig. 8, we see no particular evidence of a universal profile here. However, considerably more resolution (both in *h and N*) is needed to accurately assess the impact of angular momentum on critical collapse in this model.

momenta. We have also found evidence for a lifetime scaling law which is to be expected for type I critical solutions, and have some indications of universality. In order to produce more definitive results using our current approach, we would need to employ *many* more particles and better finite-difference resolution. Since the critical behavior in this model does *not* appear to generate structure on arbitrarily small scales, it seems unlikely that adaptive methods, such as those used in [1], would be of much help here. Thus, it may be that the development of a finite-difference code to solve the Vlasov equation directly in phase space would be the best route to more accurate results. Perhaps most importantly, this should provide a technique with better-understood, and better-controllable, convergence properties.

ACKNOWLEDGMENTS

It is our pleasure to thank W.G. Unruh, L. Lehner, and the rest of the members of the numerical relativity group at the University of British Columbia for many useful discussions. This research was supported by NSERC, the Canadian Institute for Advanced Research and the Government of the Basque Country (I.O.). Most of the calculations were performed on the vn.physics.ubc.ca Beowulf cluster, which was funded by the Canadian Foundation for Innovation.

[1] M.W. Choptuik, Phys. Rev. Lett. **70**, 9 (1993).
[2] C. Gundlach, Adv. Theor. Math. Phys. **2**, 1 (1998).
[3] G. Rein, A.D. Rendall, and J. Schaeffer, Phys. Rev. D **58**, 044007 (1998).
[4] I. Olabarrieta, M.Sc. thesis, University of British Columbia, 2000, gr-qc/0012059.
[5] S.L. Shapiro and S. Teukolsky, Astrophys. J. **298**, 34 (1985).
[6] S.L. Shapiro and S. Teukolsky, Astrophys. J. **298**, 58 (1985).
[7] S.L. Shapiro and S. Teukolsky, Astrophys. J. Lett. **292**, L41 (1985).
[8] S.L. Shapiro and S. Teukolsky, Astrophys. J. **307**, 575 (1986).
[9] J.W. York, in *Sources of Gravitational Radiation*, edited by L. Smarr (Cambridge University Press, Cambridge, England, 1979).
[10] C.W. Misner, K.S. Thorne, and J.A. Wheeler, *Gravitation* (Freeman, San Francisco, 1973).
[11] M.W. Choptuik, Ph.D. thesis, University of British Columbia, 1986.
[12] R.W. Hockney and J.W. Eastwood, *Computer Simulation Using Particles* (McGraw-Hill, New York, 1981).
[13] L.R. Petzold and A.C. Hindmarsh, ''LSODA,'' Computing and Mathematics Research Division, l-316 Lawrence Livermore National Laboratory, Livermore, CA 94550.
[14] E. Anderson *et al*, ''LAPACK Users' Guide,'' Society for Industrial and Applied Mathematics, Philadelphia, 1992 [http://www.netlib.org/lapack/lug/lapack_lug.html].
[15] M.W. Choptuik, T. Chmaj, and P. Bizoń, Phys. Rev. Lett. **77**, 424 (1996); S.H. Hawley and M.W. Choptuik, Phys. Rev. D **62**, 104024 (2000).
[16] A. Einstein, Ann. Math. **40**, 922 (1939).